Dynamics of a viscous layer flowing radially over an inviscid ocean

Samuel S. Pegler† **and M. Grae Worster**

Institute of Theoretical Geophysics, Department of Applied Mathematics and Theoretical Physics,
CMS, Wilberforce Road, Cambridge CB3 0WA, UK

We present a theoretical and experimental study of a viscous fluid layer spreading over a deep layer of denser, inviscid fluid. Specifically, we study an axisymmetric flow produced by a vertical line source. Close to the source, the flow is controlled viscously, with a balance between radial compressive stresses and hoop stresses. Further out, the flow is driven by gradients in the buoyancy force and is resisted by viscous extensional and hoop stresses. An understanding of these different fluid-mechanical relationships is developed by asymptotic analyses for early times and for the near and far fields at late times. Confirmation of the late-time, far-field behaviour is obtained from a series of laboratory experiments in which golden syrup was injected into denser solutions of potassium carbonate. We use our mathematical solutions to discuss a physical mechanism by which horizontal viscous stresses in a spreading ice shelf, such as those in West Antarctica, can buttress the grounded ice sheet that supplies it.

Key words: gravity currents, ice sheets, thin films

1. Introduction

There are very many situations in which fluids flow under gravity as thin films or gravity currents (Davis 2000; Huppert 2006). The most commonly studied cases are those in which the driving buoyancy forces are balanced by viscous shear stresses. However, there are important cases in which the shear stress is not dominant and the resisting viscous force is instead extensional. These include the glacial flow of floating ice shelves (MacAyeal 1989), the spread of crude oil on an ocean surface (DiPietro & Cox 1979), and the production of float glass, in which very viscous, molten glass spreads over the surface of essentially inviscid molten tin (Howell 1994).

Our interest stems principally from studies of marine ice sheets, such as those of West Antarctica, which are characterized by having a grounded ice sheet that is shear-dominated, coupled to a floating ice shelf in which the flow is dominantly extensional. The sheet and shelf are dynamically coupled at the freely moving line of detachment of the sheet from the bedrock called the grounding line. Most fluid-mechanical studies of marine ice sheets have been two-dimensional (Weertman 1957; Wilchinsky & Chugunov 2000; Schoof 2007; Robison, Huppert & Worster 2010), where it is found that the dynamic coupling with the ice sheet is purely hydrostatic: the dynamics of

† Email address for correspondence: ssp23@cam.ac.uk

the shelf itself has no influence on the sheet or the grounding line (Schoof 2007; Robison *et al.* 2010). However, observations of the evolution of a marine ice sheet after the collapse of an ice shelf have shown a subsequent acceleration of the grounded ice sheet that supplied it (Rignot *et al.* 2004). This suggests that ice shelves play an important role in buttressing the ice sheet, resisting the flow of grounded ice into the ocean, and preventing the grounding line from retreating.

A two-dimensional shelf provides no buttressing because the force required to push it at the grounding line is simply equal to the transmitted hydrostatic pressure of the ocean (Schoof 2007; Robison *et al.* 2010). However, in a more realistic three-dimensional setting, the force required to push the shelf at the grounding line must balance additional viscous stresses associated with the deformation of the ice shelf. In many cases, these stresses arise because the ice shelf is laterally confined, or because it meets an island, for example. These viscous stresses thus give rise to a buttressing force that forms part of the dynamic influence on the grounded sheet at the grounding line. Here, we begin to develop an understanding of the role of horizontal viscous stresses in ice shelves by studying the relatively simple case of a radially flowing ice shelf, in which buttressing comes from viscous hoop stresses. We assume that the grounding line remains fixed in space at all times and focus on comparing the buttressing force that comes from the hoop stresses to the net hydrostatic forces that would dominate the grounding-line dynamics in the absence of the shelf. In a forthcoming paper, we couple the shelf to the grounded sheet at a freely moving grounding line and analyse the effect of the ice-shelf buttressing on the dynamics of the grounding line.

Ice is understood to flow gradually under its own weight as a viscous fluid over glaciological time scales. This flow is typically modelled using Glen's flow law, which describes the ice as a shear-thinning, power-law fluid (Smith & Morland 1981). In this paper, we use a simpler Newtonian model, which can be expected to describe the same fundamental fluid-mechanical balances as Glen's flow law but within a theoretical framework that can be tested progressively in the laboratory using simple fluids. In common with previous models, we also adopt a thin-film approximation on the basis that ice shelves are typically hundreds to a few thousand metres thick but vary over length scales of hundreds of kilometres. These assumptions lead to a depth-integrated model of the shelf that forms the basis of our theoretical analyses.

In this paper, we identify several interesting new fluid-mechanical behaviours that are associated with an extensional viscous layer supplied by a source. The two-dimensional analogue of this problem has only one mode of evolution in which the current grows within a steady envelope (Robison *et al.* 2010). In contrast, we find that the axisymmetric problem involves several modes of evolution: a purely viscous extrusion near the source; convergence towards a time-dependent similarity solution far from the source; and convergence towards a steady state in a region closer to the source. The behaviour of this flow can also be contrasted strongly with those of shear-dominated viscous gravity currents flowing on a solid base (Huppert 1982) or at a fluid interface (Lister & Kerr 1989), which exhibit a single mode of evolution described by a similarity solution.

We begin in § 2 by providing a simple derivation of the model equations in general tensorial form, which we use to discuss the physical character of ice-shelf dynamics. Using a combination of analytical and numerical approaches, we proceed in § 3 to investigate the model equations in the case of an axisymmetric layer that is produced by a vertical line source at a constant volumetric rate. In a forthcoming paper (Pegler, Lister & Worster 2012), we consider the problem of a finite-volume
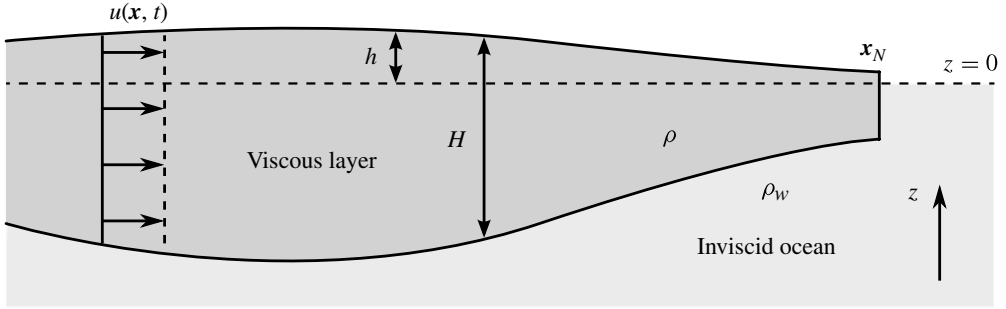
FIGURE 1. Cross-section of a viscous layer flowing over an ocean of inviscid fluid.

release. To gain confidence in the validity of the underlying assumptions of the general model, we test some of our theoretical predictions in §4 by conducting a series of laboratory experiments. We use our theoretical results in §5 to investigate the buttressing provided by an ice shelf that is produced radially at a curved grounding line.

2. General equations

Consider a thin layer of Newtonian fluid of density ρ lying on top of an ocean of stationary inviscid fluid of greater density ρ_w, as depicted in figure 1. We proceed to derive depth-integrated equations that describe the evolution of such a layer under the assumption that its thickness is much less than the characteristic length scale of its horizontal variation.

Under the influence of gravity, the layer assumes a position of vertical equilibrium in which its thickness $H(\boldsymbol{x}, t)$ and height $h(\boldsymbol{x}, t)$ above the surface of the ocean $z = 0$, are related by Archimedes' principle

$$h(\boldsymbol{x}, t) = \frac{\rho_w - \rho}{\rho_w} H(\boldsymbol{x}, t), \tag{2.1}$$

where $\boldsymbol{x} \equiv (x, y)$ is the horizontal position. Provided that (2.1) applies at all times, the motion of the layer will be predominantly horizontal and driven, for example, by gradients in its hydrostatic pressure. We assume that inertia is negligible, so that the motion is governed by the Stokes equations,

$$\nabla \cdot \boldsymbol{\sigma} = \rho g \hat{\boldsymbol{z}}, \tag{2.2}$$
$$\nabla \cdot \boldsymbol{u} = 0, \tag{2.3}$$

where $\boldsymbol{u} \equiv (u, v, w)$ is the velocity, $\boldsymbol{\sigma} \equiv -p\boldsymbol{I} + 2\mu\boldsymbol{e}$ is the stress tensor for a Newtonian fluid, p is the pressure, $\boldsymbol{e}$ is the rate-of-strain tensor, μ is the dynamic viscosity, g is the acceleration due to gravity, and $\hat{\boldsymbol{z}}$ is the vertical unit vector. Given also that the upper surface is free, and that the pressure of the ocean is given hydrostatically by $p_w = -\rho_w g z$, continuity of stress at the upper and lower surfaces determines the boundary conditions

$$\boldsymbol{\sigma} \cdot \boldsymbol{n} = \boldsymbol{0} \qquad\qquad (z = h), \tag{2.4}$$
$$\boldsymbol{\sigma} \cdot \boldsymbol{n} = \rho_w g (h - H) \boldsymbol{n} \qquad (z = h - H), \tag{2.5}$$

respectively, where $\boldsymbol{n}$ is the unit outward normal to the surface. These boundary conditions encapsulate a characteristic feature of the system, which is that neither surface is subject to tangential stress.

We proceed to integrate (2.2)–(2.3) across the depth of the flow and derive simplified equations of motion to leading order in $|\boldsymbol{\nabla} H| \sim \epsilon \ll 1$. Under this thin-film approximation, the horizontal components of (2.4)–(2.5) take the leading-order forms

$$\tilde{\boldsymbol{\sigma}} \cdot \hat{\boldsymbol{z}} = \tilde{\boldsymbol{\sigma}} \cdot \tilde{\boldsymbol{\nabla}} h \qquad\qquad (z = h), \qquad\qquad (2.6)$$

$$\tilde{\boldsymbol{\sigma}} \cdot \hat{\boldsymbol{z}} = \tilde{\boldsymbol{\sigma}} \cdot \tilde{\boldsymbol{\nabla}} (h - H) - \frac{\rho^2 g}{\rho_w} H \tilde{\boldsymbol{\nabla}} H \qquad (z = h - H), \qquad (2.7)$$

respectively, where we use the $\sim$ diacritic to denote the horizontal part of a vector or tensor. In using the $\sim$ notation for a tensor, we imply that the entries of the third row are zero, i.e. $\tilde{\sigma}_{zk} = 0$, where $k = x, y, z$, with other entries equal to those of $\boldsymbol{\sigma}$.

A balance between the viscous terms in conditions (2.6)–(2.7) shows that

$$\sigma_{iz} \sim \epsilon \sigma_{ij} \quad (i, j = x, y), \qquad\qquad (2.8)$$

at both surfaces of the layer. This implies that vertical shear stresses σ_{iz} are an order of magnitude smaller than stresses due to horizontal velocity gradients σ_{ij}. The horizontal component of (2.2) can be written

$$\tilde{\boldsymbol{\nabla}} \cdot \tilde{\boldsymbol{\sigma}} + \frac{\partial}{\partial z}(\hat{\boldsymbol{z}} \cdot \tilde{\boldsymbol{\sigma}}) = \boldsymbol{0}. \qquad\qquad (2.9)$$

Note that although (2.8) implies that vertical shear stresses are small, $\sigma_{iz} \ll \sigma_{ij}$, a scaling analysis using (2.8) shows that the second term in (2.9), which contains the vertical derivative of σ_{iz}, is in fact as significant as the first term. By balancing the deviatoric stresses in (2.8), we can also determine that

$$\frac{\partial \tilde{\boldsymbol{u}}}{\partial z} \sim \epsilon \frac{\partial \tilde{\boldsymbol{u}}}{\partial \tilde{\boldsymbol{x}}}, \qquad\qquad (2.10)$$

which shows that the horizontal velocity $\tilde{\boldsymbol{u}} \equiv (u, v)$ is independent of z to leading order.

As noted above, the thin-film approximation does not simplify the horizontal force-balance equation (2.9) directly. However, the scalings (2.8) do imply that the horizontal divergence of vertical shear stresses $\tilde{\boldsymbol{\nabla}} \cdot (\boldsymbol{\sigma} \cdot \hat{\boldsymbol{z}})$ is negligible in the vertical component of the force-balance equation (2.2), which then simplifies to

$$\frac{\partial \sigma_{zz}}{\partial z} = \rho g. \qquad\qquad (2.11)$$

We can similarly neglect the vertical-shear-stress terms in the vertical components of conditions (2.4)–(2.5), which then simplify to

$$\sigma_{zz} = 0 \qquad\qquad (z = h), \qquad\qquad (2.12)$$
$$\sigma_{zz} = -\rho g H \qquad (z = h - H). \qquad\qquad (2.13)$$

Integrating (2.11) subject to conditions (2.12)–(2.13), we obtain

$$\sigma_{zz} \equiv -p + 2\mu \frac{\partial w}{\partial z} = \rho g(z - h), \qquad\qquad (2.14)$$

which can be rearranged to show that the pressure

$$p = -\rho g(z - h) + 2\mu \frac{\partial w}{\partial z} \tag{2.15}$$

is a sum of the hydrostatic pressure and the viscous stress due to vertical extension.

We proceed to use (2.15) to simplify the horizontal force-balance equation (2.9). Integrating (2.9) across the depth of the flow, we obtain

$$\int_{h-H}^{h} \tilde{\nabla} \cdot \tilde{\sigma} \, dz + [\tilde{\sigma} \cdot \hat{z}]_{h-H}^{h} = \mathbf{0}. \tag{2.16}$$

The boundary term in (2.16) represents contributions to the horizontal force balance due to vertical shear stresses. This can be evaluated using (2.6)–(2.7) to give

$$\int_{h-H}^{h} \tilde{\nabla} \cdot \tilde{\sigma} \, dz + \tilde{\sigma} \cdot \tilde{\nabla} h - \tilde{\sigma} \cdot \tilde{\nabla}(h - H) = -\frac{\rho^2 g}{\rho_w} H \tilde{\nabla} H. \tag{2.17}$$

By swapping the order of the integral and horizontal gradient operators in the first term on the left-hand side, we can rewrite this equation as

$$\tilde{\nabla} \cdot \int_{h-H}^{h} \tilde{\sigma} \, dz = -\frac{\rho^2 g}{\rho_w} H \tilde{\nabla} H, \tag{2.18}$$

which represents a balance between the divergence of the depth-integrated horizontal stress of the layer and the horizontal component of the hydrostatic pressure of the ocean exerted on its lower surface. Using (2.15) to eliminate the pressure, we can evaluate the depth-integrated horizontal stress

$$\int_{h-H}^{h} \tilde{\sigma} \, dz \equiv \int_{h-H}^{h} -p\tilde{I} + 2\mu\tilde{e} \, dz$$
$$= -\tfrac{1}{2}\rho g H^2 \tilde{I} + 2\mu H[(\tilde{\nabla} \cdot \tilde{u})\tilde{I} + \tilde{e}], \tag{2.19}$$

in which we have used (2.3) to substitute for the rate of vertical extension $\partial w/\partial z$ in favour of the horizontal divergence of the velocity $\tilde{\nabla} \cdot \tilde{u}$, and used the fact that $\tilde{u}$ is independent of z to leading order (2.10). Substituting (2.19) into (2.18), we reduce (2.18) finally to

$$\nabla(H\nabla \cdot u) + \nabla \cdot (He) = \frac{g'}{2\nu} H\nabla H, \tag{2.20}$$

where $g' \equiv (\rho_w - \rho)g/\rho_w$ is the reduced gravity, $\nu \equiv \mu/\rho$ is the kinematic viscosity, and we have dropped the $\sim$ diacritic here for denoting horizontal parts. This equation has been derived previously by DiPietro & Cox (1979). The alternative derivation given above is a little simpler and more physically illuminating.

The governing equation (2.20) represents a balance between viscous stresses on the left-hand side and a horizontal buoyancy force on the right-hand side, which is a combination of the depth-integrated hydrostatic pressure gradient within the layer and the horizontal component of the hydrostatic pressure of the ocean exerted on its lower surface. For a given thickness profile, (2.20) is a two-dimensional elliptic equation for the horizontal velocity u that can be solved subject to suitable boundary conditions on the velocity field. Examples of such boundary conditions include the imposition of no slip at lateral sidewalls or, as detailed below, a dynamic condition at free edges of the layer.

Edges of the layer generally assume a vertical ocean–layer interface, as illustrated in figure 1. At an edge $x = x_N$, the horizontal stress of the layer must balance the hydrostatic pressure of the ocean exerted horizontally upon it. Assuming continuity of depth-integrated horizontal stress at the edge, we can determine the dynamic condition

$$\int_{h-H}^{h} \tilde{\boldsymbol{\sigma}} \cdot \boldsymbol{n} \, \mathrm{d}z = \int_{h-H}^{0} \rho_w g z \boldsymbol{n} \, \mathrm{d}z \quad (\boldsymbol{x} = \boldsymbol{x}_N), \tag{2.21}$$

where $\boldsymbol{n}$ is the unit horizontal normal to the interface. We can evaluate the left-hand side of (2.21) using expression (2.19) to give

$$(\nabla \cdot \boldsymbol{u})\boldsymbol{n} + \boldsymbol{e} \cdot \boldsymbol{n} = \frac{g'}{4\nu} H \boldsymbol{n} \quad (\boldsymbol{x} = \boldsymbol{x}_N), \tag{2.22}$$

where we have again dropped the $\sim$ diacritic. The right-hand side of this equation represents a discontinuity in the depth-integrated hydrostatic pressure between the layer and the ocean, which always acts to drive the layer outwards into the ocean.

The description of the flow is completed by a second governing equation

$$\frac{\partial H}{\partial t} + \nabla \cdot (H\boldsymbol{u}) = 0, \tag{2.23}$$

obtained by integrating the mass-conservation equation (2.3) across the depth of the flow. Given an initial thickness profile, the hyperbolic equation (2.23) defines an initial-value problem for the evolution of H. The horizontal velocity field $\boldsymbol{u}$, which appears in (2.23), can be determined at each time step from an integration of the elliptic equation (2.20). The characteristics of (2.23) are the streamlines of the flow. It is therefore necessary to impose the thickness of the layer produced at any sources.

We can think of (2.20) and (2.23) as the force-balance and continuity equations for a two-dimensional compressible viscous fluid in which the thickness H is analogous to the density of the compressible fluid. The first term on the left-hand side of (2.20) can then be interpreted as a bulk stress associated with vertical compression of the layer. The second term can be considered the usual divergence of deviatoric stresses. The effective bulk and dynamic viscosities associated with these viscous forces are each proportional to the thickness H, which shows that a given forcing leads to a deformation that is inversely proportional to H. The elliptic nature of (2.20) implies that the velocity $\boldsymbol{u}$ is determined from a global force balance. This property is fundamentally different from classical viscous gravity currents, where the velocity $\boldsymbol{u}$ at each (x, y) location can be determined from just the local thickness profile and its gradient (Huppert 1982). The flow described by (2.20) is also similar in character to that of a two-dimensional Stokes flow in the sense that forces do not necessarily decay over large distances.

Given suitable initial conditions and boundary conditions, (2.20) and (2.23) describe the general motion of a three-dimensional viscous layer subject to buoyancy forces and negligible tangential stress. We proceed to consider the illustrative example of a flow due to a vertical line source.

3. Vertical line source

Consider the flow of a floating viscous layer produced by a vertical line source that supplies the layer radially at the equilibrium flotation level, as depicted in figure 2. Let us locate the source at $r = 0$, where (r, θ) denote plane-polar coordinates. Once the
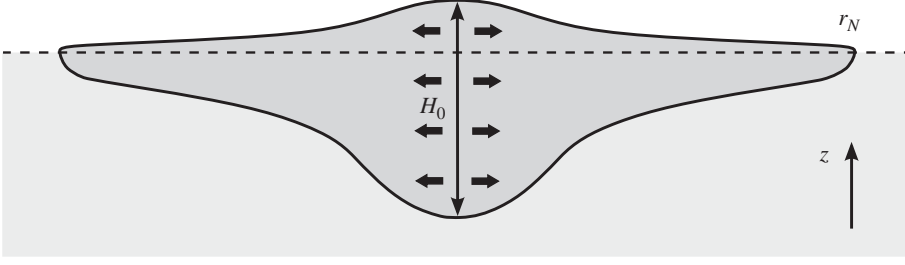
FIGURE 2. Cross-section of an axisymmetric layer produced by a vertical line source.

source has been initiated, the layer occupies the region $0 \leqslant r \leqslant r_N(t)$, where r_N denotes the radial position of the edge, or *front*, of the layer.

The radial velocity u is governed by the axisymmetric form of (2.20), namely

$$\frac{\partial}{\partial r}[H(\nabla \cdot \boldsymbol{u} + e_{rr})] + \frac{H}{r}(e_{rr} - e_{\theta\theta}) = \frac{g'}{2\nu}H\frac{\partial H}{\partial r}, \qquad (3.1)$$

where $e_{rr} = \partial u/\partial r$ and $e_{\theta\theta} = u/r$ are the rates of radial and azimuthal extension, respectively. Equation (3.1) shows that buoyancy forces act to extend the layer radially. The last term on the left-hand side represents a transverse stress due to azimuthal extension, or hoop stress, which does not feature in the two-dimensional analogue of this equation considered, for example, by Robison *et al.* (2010) and Pegler *et al.* (2012). The last two terms on the left-hand side of (3.1) equal the divergence of the anisotropic part of the deviatoric stress. For simplicity, we will refer to these two terms collectively as the hoop-stress term.

The evolution of H is governed by (2.23), which takes the axisymmetric form

$$\frac{\partial H}{\partial t} + \frac{1}{r}\frac{\partial}{\partial r}(rHu) = 0. \qquad (3.2)$$

To prescribe conditions near the source, we impose the flux condition

$$\lim_{r\to 0}(2\pi rHu) = Q_0, \qquad (3.3)$$

which implies a constant delivery of fluid at the volumetric rate Q_0. To provide an initial condition for the characteristics of (3.2), it is also necessary to impose an appropriate condition on the thickness H at $r = 0$. Trying power laws of the form $H \sim H_0 r^\alpha$ in (3.1) and (3.3), where H_0 and α are constants, we can deduce that $\alpha = 0$ is necessary for the forces in (3.1) to balance in the limit $r \to 0$. Hence, we impose

$$H = H_0 \quad (r = 0). \qquad (3.4)$$

There is one special power-law alternative to (3.4), namely $H \sim (\nu Q_0/2\pi g')^{1/2}\sqrt{6}/r$, which will be accounted for in the theoretical analyses of later sections. When combined with (3.3), condition (3.4) implies a singularity in the velocity field described by

$$\lim_{r\to 0}(ru) = \frac{Q_0}{2\pi H_0}. \qquad (3.5)$$

This singular behaviour is consistent with (3.1) provided that

$$\frac{\partial H}{\partial r} = 0 \quad (r = 0). \qquad (3.6)$$

Conditions (3.4)–(3.6) imply a purely viscous force balance near the source in which the hoop stresses balance the stresses due to vertical and longitudinal extension.

Condition (3.5) provides one condition for solution of (3.1). A second condition is given by the frontal stress condition (2.22), which takes the axisymmetric form

$$2\frac{\partial u}{\partial r} + \frac{u}{r} = \frac{g'}{4\nu}H \quad (r = r_N). \tag{3.7}$$

Conservation of mass at the front implies that it evolves kinematically according to

$$\dot{r}_N(t) = u(r_N, t). \tag{3.8}$$

We assume an initial condition in which the source begins supplying fluid at $t = 0$ into an initially empty domain, so $r_N(0) = 0$.

There are three independent dimensional parameters in the system, g'/ν, Q_0 and H_0, from which it is possible to form the time and horizontal length scales

$$T \equiv \frac{\nu}{g'H_0}, \quad L \equiv \left(\frac{\nu Q_0}{2\pi g'H_0^2}\right)^{1/2}, \tag{3.9a,b}$$

respectively. The former characterizes the time taken for buoyancy to influence a material element produced by the source. The latter, formed by combining this time scale with (3.5), characterizes the associated radius beyond which buoyancy has had significant influence on the flow. We use these scales to non-dimensionalize the system according to

$$r \equiv L\hat{r}, \quad t \equiv T\hat{t}, \quad H \equiv H_0\hat{H}, \quad u \equiv (L/T)\hat{u}. \tag{3.10}$$

On dropping hats, (3.1) and (3.2) simplify to

$$\frac{\partial}{\partial r}\left[H\left(2\frac{\partial u}{\partial r} + \frac{u}{r}\right)\right] + H\frac{\partial}{\partial r}\left(\frac{u}{r}\right) = \frac{1}{2}H\frac{\partial H}{\partial r}, \tag{3.11}$$

$$\frac{\partial H}{\partial t} + \frac{1}{r}\frac{\partial}{\partial r}(rHu) = 0. \tag{3.12}$$

Conditions (3.4), (3.5), (3.7) and (3.8) become

$$\lim_{r \to 0}(ru) = 1, \quad H(0, t) = 1, \tag{3.13a,b}$$

$$2\frac{\partial u}{\partial r} + \frac{u}{r} = \tfrac{1}{4}H, \quad \dot{r}_N = u \quad (r = r_N), \tag{3.14a,b}$$

respectively. The non-dimensional system above contains no parameters and its solution represents all instances of the dimensional system.

A numerical solution of the system above is plotted at a selection of times in figure 3. The details of the numerical method used and the calculation of the early-time similarity solution used to initialize it are described in later sections. We observe several features of the solution from figure 3. Notably, the layer is seen to converge towards a steady state in a region that extends from the source $0 \leqslant r \ll r_N$. The radial extent of this steady-state region is observed to grow in time. However, the flow in the far field $1 \ll r \leqslant r_N$ is seen to remain time-dependent at all times. These observations indicate that the rate at which the steady-state region grows in time is slower than the rate at which the front of the layer advances, so the large-scale flow is predominantly time-dependent. The log–log plot of the frontal evolution $r_N(t)$ in figure 4 shows
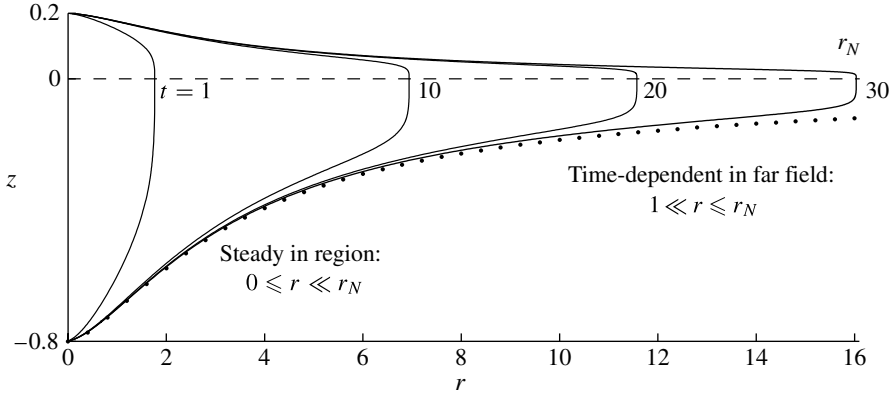
FIGURE 3. Numerical solution for the surface profiles at non-dimensional times $t = 1, 10, 20$ and 30. In drawing this figure, we chose the value $g'/g = 0.2$, which sets the proportion of the layer lying above sea level $z = 0$. At late times, we can identify a region near the source $0 \leqslant r \ll r_N$ where the flow has become steady. Our solution for the steady state is shown by the dotted curve. Beyond this steady region, the flow in the far field $1 \ll r \leqslant r_N$ is seen to remain time-dependent.
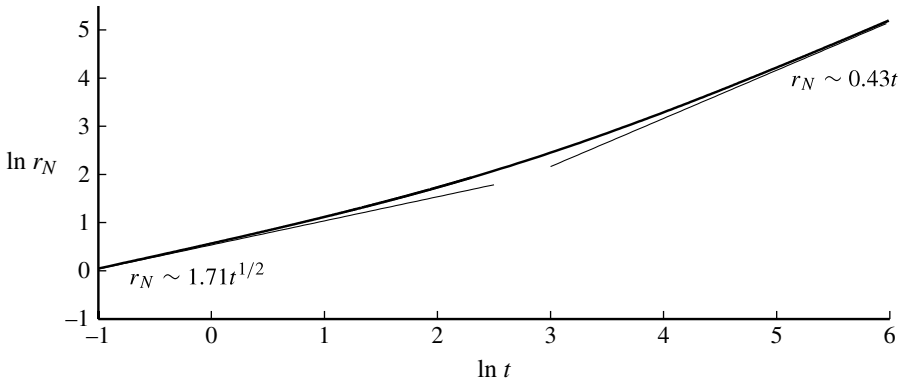

FIGURE 4. Log–log plot of the frontal evolution $r_N(t)$. The numerical calculation is shown by the thick curve. The theoretical early-time prediction $r_N \sim 1.71t^{1/2}$ and late-time prediction $r_N \sim 0.43t$, are shown by the thin curves.

a transition in power-law behaviour from $r_N \sim t^{1/2}$ at early times to $r_N \sim t$ at late times. This transition indicates the existence of separate early- and late-time modes of evolution, which we proceed to explore.

3.1. *Early evolution*

The singular velocity condition (3.13*a*) implies that viscous stresses are much greater than order unity in the region $r \ll 1$, at all times. Furthermore, (3.6) and (3.13*b*) imply that the magnitude of the horizontal buoyancy force, as represented by the right-hand sides of (3.11) and (3.14*a*), is at most order unity near the origin. Therefore, at early times, in which $r_N \ll 1$, buoyancy forces are negligible and the dominant force balance throughout the full extent of the layer is between viscous stresses alone. In the absence of the horizontal buoyancy force, this is an extrusional flow which does
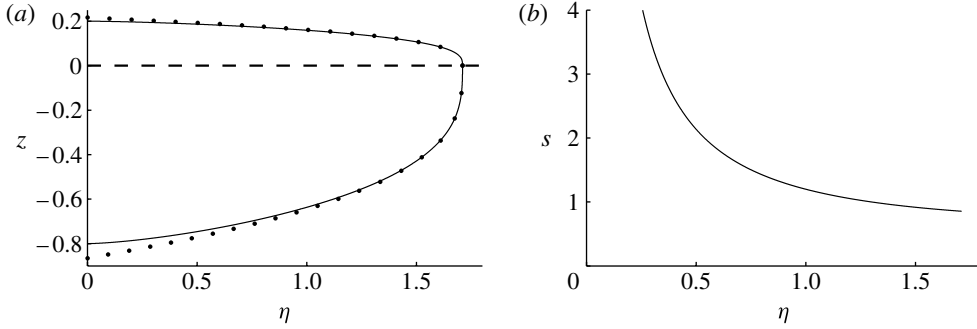
FIGURE 5. (*a*) Surface and (*b*) velocity profiles of the early-time similarity solution. The asymptotic approximation (3.21) is shown by the dotted curve in (*a*). The value $g'/g = 0.2$ was chosen for (*a*).

not conform to the time and horizontal length scales given by (3.9*a*,*b*). In order to form a horizontal length scale in this system, it is therefore necessary to incorporate an explicit dependence on time *t*, so the early-time evolution of the layer can be described by a similarity solution.

We define similarity variables by

$$\eta \equiv t^{-1/2} r, \quad H \equiv f(\eta), \quad u \equiv t^{-1/2} s(\eta), \tag{3.15}$$

such that the front evolves according to $r_N = \eta_N t^{1/2}$, where η_N is a constant. Recasting (3.11)–(3.12) in terms of these variables, we obtain

$$(fs')' + f\left(\frac{s}{\eta}\right)' + \frac{f's}{2\eta} = 0, \tag{3.16}$$

$$-\tfrac{1}{2}\eta^2 f' + (\eta f s)' = 0, \tag{3.17}$$

where the prime denotes d/dη. The boundary conditions, derived from (3.13)–(3.14), are

$$\lim_{\eta \to 0}(\eta s) = 1, \qquad f(0) = 1, \tag{3.18a,b}$$

$$s'(\eta_N) = -\tfrac{1}{4}, \qquad s(\eta_N) = \tfrac{1}{2}\eta_N, \tag{3.19a,b}$$

respectively. We use (3.17) to eliminate f'/f, and hence all presence of f, from (3.16) to leave a second-order equation for the velocity profile

$$-\eta SS'' + \tfrac{1}{2} SS' + \eta S'^2 = \tfrac{1}{2}\eta^2 (S' - \eta S''), \tag{3.20}$$

which we have written in terms of $S \equiv \eta s$ because its regularity at $\eta = 0$ is preferable for numerical purposes. We solve this equation subject to conditions (3.18*a*) and (3.19*a*,*b*) using a fourth-order Runge–Kutta scheme in which we treat η_N as a shooting parameter. Having established S, we determine f by integrating (3.17) subject to (3.18*b*) using a similar Runge–Kutta scheme.

Our solution, which is plotted in figure 5, shows that the early-time layer is fully convex with a singular slope at its front $\eta_N \approx 1.710$. We note that the no-stress condition (3.19*a*) is fundamental in determining the convex shape of the solution. By substituting a power-law form for f into (3.17), applying conditions (3.19*a*,*b*), and neglecting the higher-order terms, we can determine an asymptotic approximation for

the shape near the front,

$$f \sim 0.904 \, (\eta_N - \eta)^{1/3} \quad (\eta \to \eta_N), \tag{3.21}$$

which is shown as a dotted curve in figure 5(a). The prefactor in this equation has been determined using our numerical solution. The power is independent of the force-balance equation (3.16), which indicates that the general shape is due solely to mass conservation and the no-stress condition (3.19a).

The similarity solution calculated above describes how the layer evolves with a purely viscous force balance, which is applicable in the limit of small time. We proceed to consider how the profile evolves at larger times in which the influence of the horizontal buoyancy force becomes important.

3.2. *Influence of buoyancy*

As the extent of the layer grows, so that $r_N \sim 1$, viscous stresses in the region beyond the stress singularity at the origin decay and become comparable in magnitude to the horizontal buoyancy force. Thus, the approximation of neglecting the horizontal buoyancy force, which leads to the similarity solution calculated above, no longer applies. To determine the subsequent evolution of the layer, we solve the full initial-value problem (3.11)–(3.14) numerically using a finite-difference scheme, which we initialize using the early-time similarity solution. To ensure numerical stability of the time integration, we choose a method that evolves the nodes materially, with new nodes added periodically at the source. In using this method, the nodes become irregularly spaced over time, so to maintain second-order accuracy we use parabolic interpolation to discretize the spatial derivatives. Another advantage of this Lagrangian approach is that the growth of the numerical domain, as governed by (3.14b), is straightforwardly accounted for.

There are two important factors that influence the velocity of the layer. These are the imposition of the velocity (3.5) at the source, which drives the early-time similarity solution calculated above, and the horizontal buoyancy force, which becomes increasingly significant at larger times and distances. Given that the gradient of the layer's thickness profile is negative in the positive radial direction, buoyancy forces act to drive the layer outwards at a faster rate than would result from pushing at the source alone. One effect of this buoyancy-induced acceleration is to cause the initially convex layer to become concave at larger distances, which is shown to occur in the numerical profiles plotted in figure 3. Once the layer has propagated into the far field $r_N \gg 1$, we can expect the far-field flow to become driven predominantly by the global influence of buoyancy forces across the layer, with negligible influence from the pushing provided by the imposed velocity at the source. Therefore, given that the main role of the imposed source thickness H_0 is to control the magnitude of the velocity at the source (3.5), the flow in the far field can be expected to become independent of H_0. To test this, we plot our numerical solution at the late time $t = 50$ in figure 6 for various cases in which we change $H_0 \mapsto \alpha H_0$, for values in the range $\alpha = 0.5$–2. We observe that the profiles in the far field $r \gtrsim 10$ are approximately the same in each case, which suggests that the influence of buoyancy causes the flow to become independent of H_0 at large radii.

3.3. *Convergence towards steady flow*

It is evident from our numerical solution shown in figure 3 that the layer converges towards a steady attractor in a region near the source $0 \leqslant r \ll r_N$. This convergence shows that once the front has propagated into the far field $r_N \gg 1$, its continued
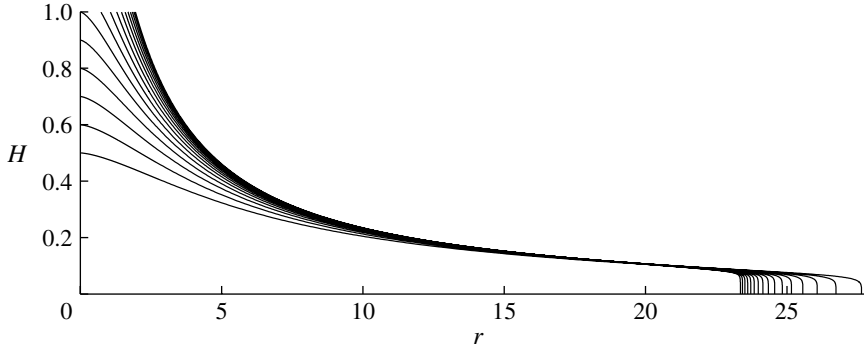
FIGURE 6. Thickness profiles at $t = 50$ for different imposed source thicknesses αH_0, where $\alpha = 0.5$–2 in intervals of 0.1. The profiles are seen to be approximately the same for $r \gtrsim 10$.

propagation has negligible influence on the near-field flow. We proceed to calculate the steady-state attractor by setting time derivatives in the system to zero.

The steady form of the mass-conservation equation (3.12) can be integrated subject to (3.13a) to give a uniform flux in the steady region, namely

$$rHu = 1. \tag{3.22}$$

Using this to eliminate u from (3.11), we obtain an equation for the steady-state thickness,

$$-HH'' + (H')^2 + \frac{HH'}{2r} = \frac{1}{4}rH^3H', \tag{3.23}$$

where $H = H(r)$, and we use a prime here to denote d/dr. Solution of this second-order equation requires two conditions, one of which is given by the entry-thickness condition (3.13b), namely

$$H(0) = 1. \tag{3.24}$$

It was noted in §3.2 that the dimensional flow in the far field $r \gg 1$ is independent of H_0. This motivates a second condition for the solution of (3.23) that requires the dimensional flow in the far field to be independent of H_0. To be independent of both the time scale (3.9a), which is necessary for the flow to be steady, and H_0, the horizontal scale (3.9b) shows that the flow must be of the form $H \sim k/r$, where k is a constant. Substituting this into (3.23), we determine that $k = \sqrt{6}$, and hence

$$H \sim \sqrt{6}/r \quad (r \to \infty). \tag{3.25}$$

This condition is consistent with no stress imposed at $r = \infty$. A constraining surface tension, for example, would imply a different far-field behaviour (see the Appendix, and Pegler *et al.* 2012).

We solve (3.23) subject to conditions (3.24) and (3.25) using a fourth-order Runge–Kutta scheme. Our solution is shown by the dotted curve in figure 3, where it is seen to match the full solution at large times and small to intermediate radii. Near the source, where the horizontal buoyancy force remains negligible at all times, the steady-state thickness profile is described by the asymptotic approximation

$$H \sim 1 - 0.135r^{3/2} \quad (r \to 0), \tag{3.26}$$

which suggests, like the similarity solution discussed in § 3.1, that the characteristic profile associated with a purely viscous force balance is convex. At larger radii, the layer turns concave as it is stretched by the buoyancy force. We can determine the velocity profile in the far field of the steady state by combining (3.22) and (3.25) to give

$$u \sim 1/\sqrt{6} \quad (r \to \infty). \tag{3.27}$$

This asymptote is uniform, which implies that there is a balance between the two competing effects of deceleration due to radial spreading and acceleration due to buoyancy-induced extension, in the far field of the steady state.

As we have observed, the steady region develops at a rate that is slower than the rate at which the front of the layer advances. As time proceeds, the steady region therefore occupies a progressively smaller proportion of the layer, so that the layer eventually becomes predominantly time-dependent. We proceed to consider the large-scale, time-dependent flow of the layer at late times.

3.4. *Large-scale evolution*

It was observed in § 3.2 that the flow loses knowledge of the imposed source thickness H_0 after travelling a distance characterized dimensionally by the length scale L, defined by (3.9b). The flow is therefore independent of H_0 in the limit of large radius $r \gg 1$. To form a horizontal length scale without H_0, it is necessary to incorporate an explicit dependence on time t. The large-scale flow can therefore be described by a similarity solution.

We define similarity variables by

$$\xi \equiv t^{-1}r, \quad H \equiv t^{-1}f(\xi), \quad u \equiv u(\xi), \tag{3.28}$$

such that the front evolves according to $r_N = \xi_N t$, where ξ_N is a constant. Transforming (3.11)–(3.12) in terms of these variables, we obtain

$$\left[f \left(2u' + \frac{u}{\xi} \right) \right]' + f \left(\frac{u}{\xi} \right)' = \frac{1}{2} f f', \tag{3.29}$$

$$(\xi f u)' = \xi^2 f' + \xi f, \tag{3.30}$$

respectively, where we use a prime here to denote $\mathrm{d}/\mathrm{d}\xi$. The dynamic and kinematic conditions at the front (3.14a,b) become

$$2u'(\xi_N) + u(\xi_N)/\xi_N = \tfrac{1}{4} f(\xi_N), \tag{3.31}$$

$$u(\xi_N) = \xi_N. \tag{3.32}$$

As shown in figure 3, the large-scale flow emerges from the steady-state region discussed in § 3.3. The large-scale flow overlaps the far field of the steady state in an intermediate region $1 \ll r \ll r_N$. We therefore impose the matching conditions

$$f \sim \sqrt{6}/\xi \quad (\xi \to 0), \tag{3.33}$$

$$u(0) = 1/\sqrt{6}. \tag{3.34}$$

We solve the system described by (3.29)–(3.34) numerically using a fourth-order Runge–Kutta scheme. To avoid numerical errors caused by starting the integration at the edges of the domain, where the solution contains singularities in high-order derivatives, we choose a method that shoots over the values of f, u and u' from an
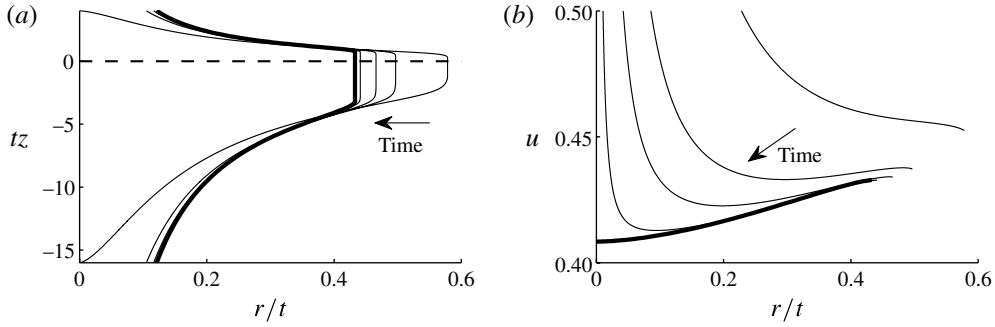
FIGURE 7. (*a*) Surface and (*b*) velocity profile evolution plotted in similarity coordinates (3.28) at times 20, 50, 100 and 400, to show the late-time convergence of the solution towards the large-scale similarity solution (bold). Note that the spatial coordinates on the axes depend on time *t*. The value $g'/g = 0.2$ was chosen for (*a*).

arbitrary point lying between the source and the front. Our solution is shown by the bold curves in figure 7. In the same figure, we also plot our full numerical solution, which shows that it is attracted towards the similarity solution at late times.

By evaluating (3.30) at $\xi = \xi_N \approx 0.433$, and substituting conditions (3.31) and (3.32), we can deduce that the thickness at the front is described by

$$f(\xi_N) = 4. \tag{3.35}$$

This result is consistent with a flattening of the initially convex front towards a vertical interface, which is seen to occur in figures 3, 7(*a*), and experimentally in figure 9.

4. Experimental analysis

Our objective is to use the theoretical framework developed in this paper to address the problem of a grounding line influenced by three-dimensional stresses in an ice shelf. To gain confidence in this framework, we have conducted a series of laboratory experiments with which to compare aspects of the theoretical predictions.

4.1. *Experimental system*

Our experiments were conducted in a circular Perspex tank of approximate diameter 90 cm, shown schematically in figure 8. We used pure or diluted golden syrup of density $\rho \approx 1.4$ g cm^{-3} and viscosity $\nu \approx 50$–550 cm^2 s^{-1} to model the floating viscous layer. For the ocean, we used an aqueous solution of potassium carbonate, which has a significantly lower viscosity than golden syrup, but can have a greater density of up to $\rho_w \approx 1.56$ g cm^{-3}.

A delivery system composed of a reservoir connected to a cylindrical delivery tube was used to provide a constant flux of golden syrup at the centre of the tank. We used delivery tubes of different inner diameters of 2 and 3 cm. To control the initialization of the delivery, we secured the top of the reservoir to a horizontal platform that could be raised or lowered vertically using a crank-operated mechanism.

In Pegler *et al.* (2012), we show that a constraining surface tension can prevent the thickness of the layer decreasing below a threshold value. To indicate the potential importance of surface tension in our experiments, we perform a scaling analysis in the Appendix to determine a characteristic horizontal length scale beyond which we expect capillary effects to play an important role. This analysis suggests that an experiment
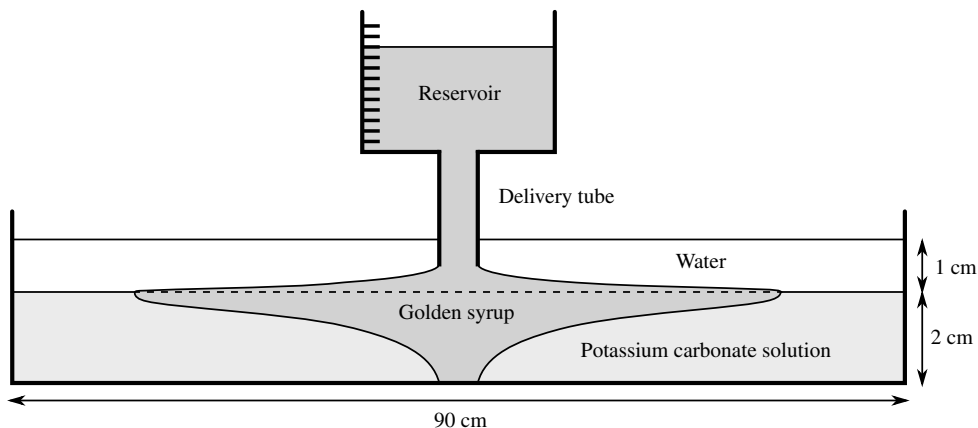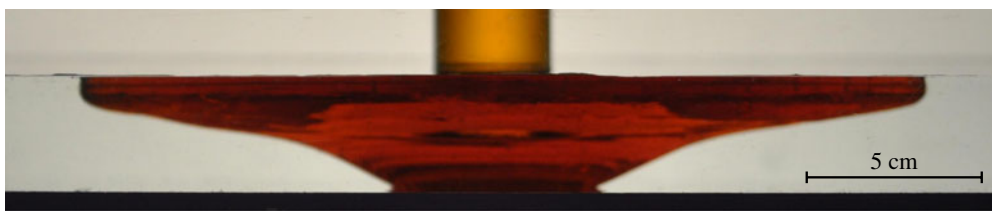
FIGURE 8. Cross-section of our experimental system.

FIGURE 9. (Colour online available at journals.cambridge.org/flm) Side-view photograph of our experiment. An upper layer of water was not included in the experiment performed to take this photograph because of the optical distortion it causes. The observed vertical front is consistent with the late-time theoretical prediction (3.35).

using golden syrup and potassium carbonate solution with air above would be strongly influenced by capillary effects. This was confirmed by the results of some preliminary experimental runs. To effectively eradicate these capillary effects, we arranged a layer of water of density $\rho_a \approx 1.00$ g cm^{-3} above the solution, such that the syrup flowed along the interface between the solution and the water. The presence of the inviscid upper layer could be accommodated straightforwardly into the theoretical model by using a generalized formula for the reduced gravity

$$g' \equiv \frac{(\rho_w - \rho)(\rho - \rho_a)}{(\rho_w - \rho_a)\rho} g. \tag{4.1}$$

Before each experiment, we measured the delivery flux Q_0 by measuring the time taken for the delivery system to supply a certain volume of syrup, to an accuracy of $\pm 0.01\,\%$. We also measured the viscosity of the syrup using a falling-sphere method, to an accuracy of $\pm 5\,\%$, and the density of the potassium carbonate solution using a hydrometer, to an accuracy of $\pm 1\,\%$. To set up the experiment, the delivery tube was lowered to the base of the tank and filled with golden syrup to a specified head in the reservoir. We then filled the tank with potassium carbonate solution to a depth of approximately 2 cm, and used a sponge-boat method to arrange a layer of water of approximate depth 1 cm above the solution. The interface between these layers was smeared by the filling process over a vertical extent of a few millimetres. To initialize the flow of syrup, we raised the reservoir to a point where the base of the delivery

Experiment	ν (cm^2 s^{-1})	g' (cm s^{-2})	Q_0 (cm^3 s^{-1})	t_s (s)	ν/g' (cm s)	H_s (cm)
(*a*)	73	30.9	7.5	30	2.4	0.3
(*b*)	329	28.9	9.5	60	11.4	0.8
(*c*)	436	30.1	6.9	120	14.5	0.5
(*d*)	271	28.4	2.1	100	9.5	0.4
(*e*)	530	13.0	6.4	>370	40.8	<0.5

TABLE 1. Parameter values used in our experiments. The last three columns display quantities that we use to estimate the thickness of the current $H_s \equiv 4\nu/g't_s$ at the approximate time t_s when the experimental evolution is first observed to disagree significantly with the theoretical prediction.

tube lay just above the interface between the water and the solution. We chose the depths of the ocean and the values of g' sufficiently small that the syrup made contact with the base of the tank in the vicinity of the source at all times. This pinned the layer's centre, preventing it drifting, and ensuring a strongly axisymmetric layer that remained centred at the source at all times. As the experiment progressed, a constant flux of syrup was maintained by keeping a constant head in the reservoir. We recorded the experiment using a digital camera directed to view the underside of the tank via an angled mirror placed beneath it. These recordings were analysed later to determine the evolution of the front in time. Table 1 shows the parameter values used in our experiments. A side-view photograph of an experiment is shown in figure 9.

4.2. *Experimental results*

Our experimental source differed slightly from the idealized vertical line source studied theoretically because the syrup remained in contact with the base of the tank over a short distance of a few centimetres in the vicinity of the source, as shown in figure 9. We therefore expect the initial transients of the experimental evolutions to differ from those of our theoretical predictions at early times. However, we do expect the experimental current produced by the source to converge towards the large-scale similarity solution calculated in § 3.4 because its form is independent of conditions close to the source.

To test this, we compare the experimental frontal location r_N to the late-time prediction for the evolution of the front, namely

$$r_N \sim 0.43 \left(\frac{g'Q_0}{2\pi\nu} \right)^{1/2} t \quad (t \to \infty), \tag{4.2}$$

which we determined in § 3.4. The evolution of the front of the layer measured from the centre of the delivery tube is plotted for each of our experiments in figure 10. For each experiment, we perform a time shift of the experimental evolution to provide an effective comparison with the late-time prediction (4.2). Apart from this time shift, we use no adjustable parameters in comparing our experiments with the prediction (4.2).

Our experiments span kinematic viscosities ν from 73 to 530 cm^2 s^{-1}, reduced gravities g' from 13.0 to 30.9 cm^2 s^{-1}, and input fluxes Q_0 from 2.1 to 9.5 cm^2 s^{-1}. In each case, the experimental evolution is observed to converge towards the late-time prediction (4.2) with good agreement persisting for a substantial time after the injection is initiated. No significant initial transient occurs in cases (*a*) or (*d*) in which the front evolves at approximately the same velocity as the prediction (4.2) at
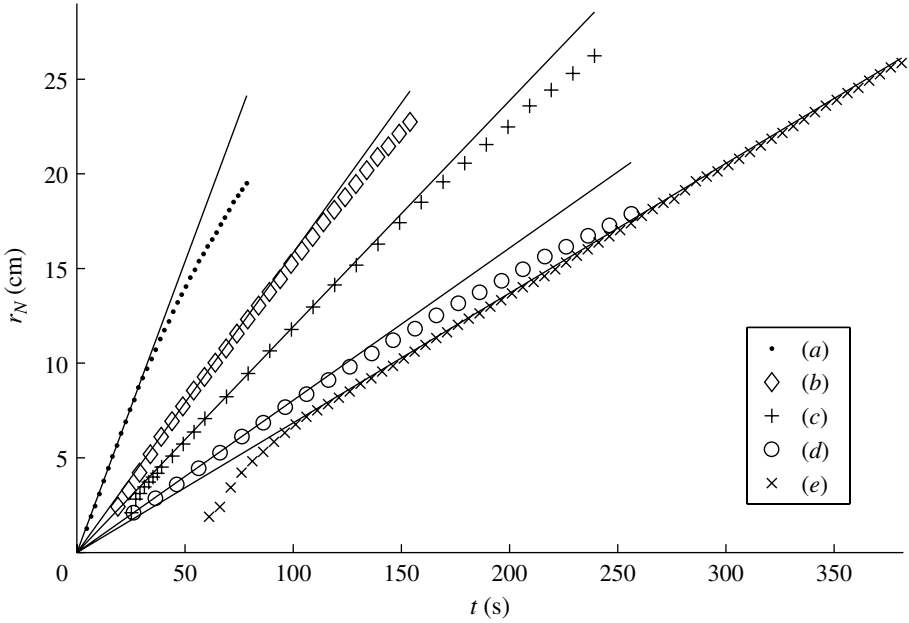
FIGURE 10. Comparison of the experimental evolution of the front and the late-time theoretical prediction $r_N = 0.43 \, (g' Q_0/2\pi\nu)^{1/2} \, t$, for each experiment. The experimental evolutions have been time shifted to provide an effective comparison with the late-time prediction.

the first measured location. In contrast, experiment (*e*) undergoes a significant initial transient in which the front evolves faster than the velocity of the prediction (4.2) for approximately 50 s after the injection is initialized.

Beyond a certain time, different in each experiment, the front is observed to propagate slower than the prediction (4.2) in experiments (*a*)–(*d*). We suspect that this late-time disagreement is a consequence of the smeared density profile at the interface between the water and the solution, which we assumed to be perfectly sharp in our idealized theoretical calculation. Once the thickness of the layer becomes comparable to the vertical scale of the smearing, the magnitude of buoyancy-induced extension, and hence the propagation speed, become smaller than predicted.

We can observe that the approximate time t_s when the late-time disagreement first arises is different in each experiment. These approximate times t_s are shown in table 1. For example, experiment (*a*) begins to disagree at $t_s \approx 30$ s, which is earlier than the typical time of disagreement $t_s \approx 60$–110 s for experiments (*b*)–(*d*). In experiment (*e*), no significant late-time disagreement occurs over the running time of the experiment, so $t_s > 350$ s. Assuming that the vertical scale of the smearing is similar in each experiment, the late-time prediction (3.35), namely

$$H(r_N, t) \sim \frac{4\nu}{g' t} \quad (t \to \infty), \tag{4.3}$$

implies that greater values of the ratio ν/g' lead to a longer time t_s before the thickness of the layer becomes comparable to the vertical scale of the smearing. The value of ν/g' for each experiment is shown in table 1. The fact that ν/g' is greatest in experiment (*e*), smallest in experiment (*a*), and approximately equal in experiments

(b)–(d), suggests that the observed differences in t_s are indeed due to variations in the rate at which the thickness of the layer becomes comparable to the vertical scale of the smearing. By combining the observed times t_s with the values of ν/g' in each experiment, we use (4.3) to estimate the vertical scales of smearing $H_s \equiv 4\nu/g't_s$ shown in table 1. These scales are consistent with our visual observations of a smeared interface of a few millimetres.

5. Ice-shelf buttressing

We can use the theoretical model considered in §3 to investigate how the hoop stresses in a spreading ice shelf lead to buttressing of a grounded ice sheet.

In a marine ice sheet, the *back force* exerted by the ice shelf onto the grounded ice sheet at a point on the grounding line x_G can be measured by the depth-integrated normal stress

$$F \equiv -\int_{h-H}^{h} \sigma_{nn}\,\mathrm{d}z \quad (x = x_G), \tag{5.1}$$

where n is the unit horizontal normal to the grounding line. In the case of a two-dimensional shelf, Schoof (2007) shows that $F = \rho^2 g H^2/2\rho_w \equiv F_w$, which is the equivalent back force provided by a column of ocean fluid lying adjacent to the grounding line. A two-dimensional shelf therefore provides no buttressing itself and simply transmits the hydrostatic pressure of the ocean. We proceed to show that the additional hoop stresses in a radially flowing shelf lead to a back force that is different from F_w.

Consider a shelf produced radially at a circular grounding line $r = r_G$ with frontal position $r = r_N$. The integral in (5.1) can be evaluated using (2.19) to show that the back force at the grounding line is given by

$$F = \tfrac{1}{2}\rho g H^2 - 2\mu H(\nabla \cdot u + e_{rr}) \quad (r = r_G), \tag{5.2}$$

which is a sum of the depth-integrated hydrostatic pressure of the layer and the local viscous stresses due to vertical and longitudinal extension, respectively. By integrating the force-balance equation (3.1) from $r = r_G$ to $r = r_N$, and applying the dimensional forms of (3.25) and (3.27) to evaluate the far-field boundary terms, we can determine that the viscous contribution to (5.2) is given by

$$2\mu H(\nabla \cdot u + e_{rr}) = \frac{1}{2}\rho g'H^2 + 2\mu \int_{r_G}^{\infty} H\frac{\partial}{\partial r}\left(\frac{u}{r}\right)\mathrm{d}r \quad (r = r_G), \tag{5.3}$$

which shows that it equals the combination of the transmitted buoyancy force and a global integral of hoop-stress contributions in front of the grounding line. Substituting (5.3) into (5.2), we determine that the back force

$$F = F_w - 2\mu \int_{r_G}^{\infty} H\frac{\partial}{\partial r}\left(\frac{u}{r}\right)\mathrm{d}r \quad (r = r_G) \tag{5.4}$$

has two contributions: the transmitted hydrostatic pressure of the ocean F_w, and the force required to balance the viscous hoop stresses throughout the shelf.

Let us define the *buttressing* of the shelf as the component of (5.4) that is due to the viscous forces in the shelf, namely

$$B \equiv F - F_w = -2\mu \int_{r_G}^{\infty} H\frac{\partial}{\partial r}\left(\frac{u}{r}\right)\mathrm{d}r. \tag{5.5}$$

If the shelf were to collapse, B equals the resulting change in force exerted by the shelf onto the grounded sheet and hence measures the buttressing provided by the shelf. Equation (5.5) shows that the hoop stresses in the shelf are solely responsible for the buttressing of the sheet.

For demonstration, we proceed to calculate the buttressing B for the steady-state radial shelf that is produced at constant flux Q_0, at constant thickness H_0 and at the fixed circular grounding line $r = r_G$. To apply this analysis more readily to the geophysical setting, we can interpret r_G as the radius of curvature of the velocity contours of the ice flow across the grounding line.

Let us adopt the non-dimensional variables (3.10). Then the thickness profile of the steady-state shelf is given by solution of the steady-state equation (3.23) subject to the far-field condition (3.25), and the generalized entry condition

$$\hat{H}(\hat{r}_G) = 1, \tag{5.6}$$

where $\hat{r}_G \equiv r_G/L$ is the non-dimensional grounding-line radius. Having established $\hat{H}$ by solving (3.23) subject to conditions (5.6) and (3.25) using a fourth-order Runge–Kutta scheme, we compute using quadrature the non-dimensional form of (5.5), namely

$$\hat{B}(\hat{r}_G) \equiv \frac{B}{\rho g' H_0^2} = -2 \int_{\hat{r}_G}^{\infty} \hat{H} \frac{\partial}{\partial \hat{r}} \left(\frac{1}{\hat{r}^2 \hat{H}} \right) \, \mathrm{d}\hat{r}, \tag{5.7}$$

where we have used (3.22) to substitute for $\hat{u}$ in favour of $\hat{H}$.

In the absence of the shelf, the grounding line is controlled by a balance between the viscous stresses in the sheet and the net hydrostatic forces between the front of the ice sheet and the ocean adjacent to it (Schoof 2007; Robison et al. 2010). This net hydrostatic force can be evaluated dimensionally as

$$F_0 \equiv F_w - \int_{h-H}^{h} -\rho g(z - h) \, \mathrm{d}z = -\tfrac{1}{2} \rho g' H_0^2 \quad (r = r_G). \tag{5.8}$$

To determine the relative importance of the buttressing $\hat{B}$ in the balance of forces at the grounding line, we compare it to the non-dimensional form of (5.8), given by $\hat{F}_0 \equiv F_0/\rho g' H_0^2 = -1/2$, by plotting the ratio $\hat{B}/|\hat{F}_0|$ in figure 11 for different values of $\hat{r}_G$. It is observed that buttressing $\hat{B}$ is dominant in the limit $\hat{r}_G \to 0$, is significant for $\hat{r}_G \lesssim 3$, and has a relative magnitude of less than 2 % for $\hat{r}_G > 10$. The singular behaviour of $\hat{B}$ is described by the asymptote

$$\hat{B} \sim 2\hat{r}_G^{-2} - 0.81\hat{r}_G^{-1/2} \quad (\hat{r}_G \to 0), \tag{5.9}$$

which we can determine by substituting (3.26) into (5.7), evaluating the integral, and neglecting the higher-order terms. For $\hat{r}_G \gtrsim 5.7$, the buttressing $\hat{B}$ is seen to become negative. This is curious because it implies that the shelf pulls the sheet, which is contrary to the common expectation that ice shelves provide a back force that constrains the flow at the grounding line. To explain this change in sign, we first note that the velocity profiles increase with radius for $\hat{r}_G > \sqrt{6}$, as shown in figure 12. For $\hat{r}_G \gtrsim 5.7$, this buoyancy-induced acceleration of the flow is sufficiently large that the azimuthal extension u/r first increases close to the grounding line. The integrand of (5.5), which represents the divergence of the anisotropic stress, then becomes negative close to the grounding line and this implies a pulling of the sheet at the grounding line.
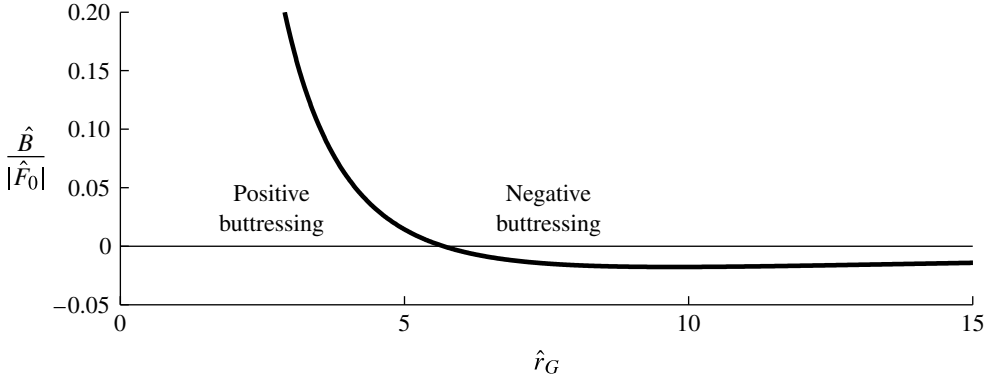
FIGURE 11. Ratio of the buttressing provided by the hoop stresses in a steady-state axisymmetric shelf and the magnitude of the depth-integrated hydrostatic pressure discontinuity at the grounding line if the shelf were absent, $\hat{F}_0 = -1/2$, plotted against the non-dimensional grounding-line radius, $\hat{r}_G \equiv r_G/L$.
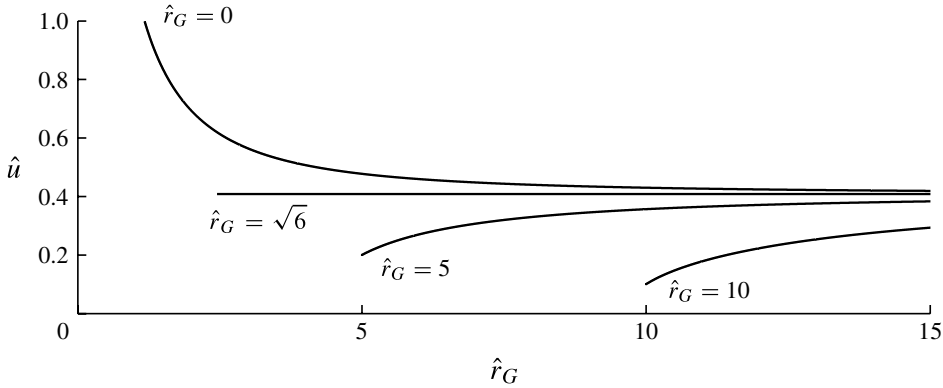

FIGURE 12. Velocity profiles of the steady axisymmetric shelf for non-dimensional grounding-line radii $\hat{r}_G = 0, \sqrt{6}, 5$ and 10.

The length scale $L \equiv (\nu Q_0/2\pi g'H_0^2)^{1/2}$ characterizes the radius of curvature of the velocity contours across the grounding line below which the hoop stresses in the shelf lead to significant buttressing. In considering the geophysical setting, let us assume that the (effective) kinematic viscosity of the ice is given by Glen's flow law,

$$\nu = \frac{1}{2\rho}A^{-1/3}\dot{\gamma}^{-2/3}, \tag{5.10}$$

where $\dot{\gamma} \equiv \sqrt{\boldsymbol{e}\colon\boldsymbol{e}/2}$ is the rate of deformation, and A is a temperature-dependent, rheological constant (Smith & Morland 1981). Assuming also that the flux is given by $Q_0 = 2\pi r_G H_0 u_0$, where u_0 is the characteristic velocity of the flow across the grounding line, and that $\dot{\gamma} \sim u_0/L$, we can show by performing a scaling analysis that the characteristic radius of curvature below which hoop stresses are important is

$$r_G \sim \frac{u_0}{A\,(\rho g'H_0)^3}. \tag{5.11}$$

Given an ice-shelf thickness $H_0 \approx 300$ m, velocity $u_0 \approx 300$ m year^{-1}, rheological constant $A \approx 10^{-25}$ s^{-1} Pa^{-3}, density $\rho \approx 900$ kg m^{-3}, and reduced gravity $g' \approx 1.0$ m s^{-2}, we can evaluate (5.11) to be $r_G \approx 5$ km. From this, we can determine that it is feasible for the buttressing due to the hoop stresses in an ice shelf to have a significant influence on the dynamics of the grounding line for horizontal and vertical length scales that are consistent with our thin-film assumption. It is likely however, that more significant buttressing derives from horizontal viscous shear stresses in many cases.

6. Conclusions

We have developed a model for a three-dimensional layer of viscous fluid that flows over a denser inviscid fluid, tested its predictions using simple laboratory experiments, and elucidated the mechanism by which horizontal viscous stresses in an ice shelf lead to buttressing of the grounded ice sheet. Our solution for the flow due to a vertical line source shows that the flow near the source converges towards a steady state with the large-scale flow beyond the steady region converging towards a similarity solution. We identified the important horizontal length scale $L \equiv (\nu Q_0 / 2\pi g' H_0^2)^{1/2}$ that characterizes scales on which the buoyancy force is significant. The flow was shown to lose knowledge of the imposed source thickness H_0 after propagating a distance characterized by L. Good agreement between the results of our experiments and the predictions of the theory provides confidence in the underlying assumptions of the general model.

We used our solutions to discuss a mechanism by which the hoop stresses in an ice shelf lead to buttressing of the grounded ice sheet that supplies it. By calculating the back force at fixed grounding-line positions, we determined that viscous hoop stresses in the shelf have the potential to dominate the dynamic influence on the grounded sheet. The length scale L was shown to characterize the radius of curvature of the grounding line below which hoop stresses lead to a significant contribution to the back force exerted on the sheet. For sufficiently large grounding-line radius, $r_G \gtrsim 6L$, the buttressing becomes negative, so that the shelf pulls the sheet rather than constrains it.

To understand the effect of these three-dimensional viscous stresses on the evolution of the ice sheet and the migration of the grounding line, it is necessary to consider the stresses in the ice sheet and its dynamical coupling with the shelf at a freely moving grounding line. This broader problem forms the subject of a future paper in preparation.

Appendix. Significance of surface tension

To determine the potential significance of surface tension in our experiments, we model its leading-order influence and compare its magnitude to that of the buoyancy force by performing a scaling analysis. For a thin layer, Howell (1994) shows that the leading-order effect of surface tension is to include an additional term, $-\gamma \boldsymbol{n}$, on the right-hand side of the dynamic condition (2.22). The constant $\gamma \equiv \gamma_{va} + \gamma_{vw} - \gamma_{aw}$

is a coefficient of total surface tension composed of the interfacial surface tensions between the layer and the air, γ_{va}, the layer and the ocean, γ_{vw}, and the ocean and the air, γ_{aw}. Condition (3.7) is then replaced by

$$2\frac{\partial u}{\partial r} + \frac{u}{r} = \frac{g'}{4\nu}H - \frac{\gamma}{2\mu H} \quad (r = r_N). \tag{A 1}$$

In Pegler *et al.* (2012), we use (A 1) to analyse the influence of surface tension in the case of a finite-volume release, where it is found to prevent the layer thinning below a threshold thickness $H_c \equiv \sqrt{2\gamma/\rho g'}$.

In the absence of surface tension, the late-time prediction (4.3) implies that the thickness at the front thins in time. The surface tension, which is represented by the second term on the right-hand side of (A 1), can therefore be expected to balance the buoyancy force after sufficient time has elapsed. Once this balance is established, the thickness at the front attains the equilibrium thickness $H_c \equiv \sqrt{2\gamma/\rho g'}$. Assuming that $H \sim H_c$, and that the viscous forces on the left-hand side of (A 1) balance the driving forces on the right-hand side, we can determine that the length scale

$$L_c \equiv \left(\frac{\mu Q_0}{2\pi\gamma}\right)^{1/2} \tag{A 2}$$

characterizes the distance from the source beyond which the layer has thinned sufficiently for capillary forces to significantly affect its dynamics.

We evaluate L_c for an experiment that involves golden syrup flowing over a layer of aqueous potassium carbonate solution with air above it. The coefficient of surface tension for the interface between golden syrup and air is $\gamma_{va} \approx 78$ dyn cm^{-1} at typical room temperatures. Assuming that the surface tension between the syrup and the solution is negligible $\gamma_{vw} \approx 0$, and that the surface tension between the air and the solution is approximately the same as that between air and water $\gamma_{aw} \approx 73$ dyn cm^{-1}, we obtain $\gamma \equiv \gamma_{va} + \gamma_{vw} - \gamma_{aw} \approx 5$ dyn cm^{-1}. For parameter values used in our experiments, this corresponds to a range of $L_c \approx 5$–12 cm for (A 2). These values are comparable to the radii of currents produced in our experimental system, so we can expect capillary effects to have a significant influence on the flow if we use an ocean of potassium carbonate solution with air above. This motivated our decision to arrange a layer of water on top of the potassium carbonate solution, which we expect to have eradicated the effects of surface tension and achieved $\gamma \approx 0$.

REFERENCES

DAVIS, S. H. 2000 Interfacial fluid dynamics. In *Perspectives in Fluid Dynamics: A Collective Introduction to Current Research*, (ed. G. K. Batchelor, H. K. Moffatt & M. G. Worster), pp. 1–52. Cambridge University Press.

DIPIETRO, N. D. & COX, R. G. 1979 The spreading of a very viscous liquid on a quiescent water surface. *Q. J. Mech. Appl. Maths* **32**, 355–381.

HOWELL, P. D. 1994 Extensional thin layer flows. PhD thesis, University of Oxford.

HUPPERT, H. E. 1982 The propagation of two-dimensional and axisymmetric viscous gravity currents over a rigid horizontal surface. *J. Fluid Mech.* **121**, 43–58.

HUPPERT, H. E. 2006 Gravity currents: a personal perspective. *J. Fluid Mech.* **554**, 299–322.

LISTER, J. R. & KERR, R. C. 1989 The propagation of two-dimensional and axisymmetric viscous gravity currents at a fluid interface. *J. Fluid Mech.* **203**, 215–249.

MACAYEAL, D. R. 1989 Large-scale ice flow over a viscous basal sediment: theory and application to Ice Stream B, Antarctica. *J. Geophys. Res.* **94**, 4071–4087.

PEGLER, S. S., LISTER, J. R. & WORSTER, M. G. 2012 Release of a viscous power-law fluid over a denser inviscid ocean. *J. Fluid Mech*, doi:10.1017/jfm.2012.91.

RIGNOT, E., CASASSA, G., GOGINENI, P., KRABILL, W., RIVERA, A. & THOMAS, R. 2004 Accelerated ice discharge from the Antarctic Peninsula following the collapse of Larsen B ice shelf. *Geophys. Res. Lett.* **31**, L18401.

ROBISON, R. A. V., HUPPERT, H. E. & WORSTER, M. G. 2010 Dynamics of viscous grounding lines. *J. Fluid Mech.* **648**, 363–380.

SCHOOF, C. 2007 Marine ice sheet dynamics. Part 1 The case of rapid sliding. *J. Fluid Mech.* **573**, 27–55.

SMITH, G. D. & MORLAND, L. W. 1981 Viscous relations for the steady creep of polycrystalline ice. *Cold Reg. Sci. Technol.* **5**, 141–150.

WEERTMAN, J. 1957 Deformation of floating ice shelves. *J. Glaciol.* **3**, 38–42.

WILCHINSKY, A. V. & CHUGUNOV, V. A. 2000 Ice stream–ice shelf transition: theoretical analysis of two-dimensional flow. *Ann. Glaciol.* **30**, 153–162.